Journal of Electroanalytical Chemistry 1003 (2026) 119759

Contents lists available at ScienceDirect

Journal of Electroanalytical Chemistry

journal homepage: www.elsevier.com/locate/jelechem

Design of polypyrrole-modified NiCo-LDH electrocatalysts for high-performance seawater electrolysis

Ziqi Wang [a,1], Xiaomei Wang [b,1], Zhihao Xia [a], Tian Tian [a], Yucai Li [a,*], Shiwei Song [a], Jian Wang [a], Fang Hu [b,*], Lihua Miao [c,*]

[a] School of New Energy, Shenyang Institute of Engineering, Shenyang, Liaoning, CN 110136, PR China
[b] School of Materials Science and Engineering, Shenyang University of Technology, Shenyang 110870, PR China
[c] School of Medical Information Engineering, Shenyang Medical College, Shenyang, Liaoning 110043, PR China

ARTICLE INFO

Keywords:
NiCo-LDH
Hydrogen evolution reaction
Oxygen evolution reaction
Water electrolysis

ABSTRACT

Among numerous transition metal hydrogen evolution reaction catalysts, nickel-based catalysts have garnered significant attention for their relatively better electrocatalytic activity. The hydrothermal-electrodeposition method provides an effective route for preparing relatively better nickel-based catalysts. Building upon this, this study successfully synthesised NiCo-LDH@PPy. Under alkaline conditions, NiCo-LDH@PPy-100 exhibits a HER overpotential of 210.7 mV at 50 mA cm^{-2} and a double-layer capacitance of 0.013 mF cm^{-2}. Following 28 h of constant current testing, XPS experiments revealed minimal changes in elemental composition, suggesting good stability of the sample under electrochemical conditions. To more accurately evaluate the practical application potential of the catalyst, when the electrolyte was switched to alkaline seawater, NiCo-LDH@PPy-100 exhibits HER and OER overpotentials of 223.7 mV and 270 mV at 50 mA cm^{-2}, respectively. The overall water splitting potential was 1.64 V at a current density of 10 mA cm^{-2}, and the catalyst demonstrated excellent electrochemical stability during 50 h of continuous testing, offering a viable alternative to precious metal catalysts for seawater splitting.

1. Introduction

Renewable energy's intermittency requires energy storage and conversion and hydrogen (143 MJ/kg high energy density, with no carbon dioxide emissions) from electrolysis turns its electricity into chemical energy for the green hydrogen economy [1–6]. However, industrial water electrolysis for hydrogen production suffers from low energy conversion efficiency primarily due to the slow four-electron transfer kinetics of the anode oxygen evolution reaction (OER) [7–9]. Currently, Noble metal-based catalysts (Pt for the cathode, IrO_2/RuO_2 for the anode) exhibit relatively higher activity compared to non-noble metal-based catalysts. However, their extremely low abundance in the Earth's crust leads to excessively high costs, making them unsuitable for the commercial application of water electrolysis technology [10–14]. Against this backdrop, transition metal compounds based on Earth-abundant elements—particularly iron, cobalt, and nickel-based materials-demonstrate significant potential to replace precious metal catalysts. This stems from their tunable d-orbital electronic structure, excellent conductivity, intrinsic stability under alkaline conditions, and ease of large-scale preparation [15–18].

Nickel-based layered double hydroxides (Ni-LDH), with their unique two-dimensional layered structure, tunable chemical composition, and relatively more electrochemical activity, demonstrate significant potential in the field of electrocatalytic water splitting [19–21]. NiFe-LDH shows efficient OER performance due to its intrinsic electronic structure and the presence of catalytically active metal centers. Similarly, NiFe and CoFe layered double hydroxides exhibit relatively more electrocatalytic activity for alkaline OER in water splitting [22–26]. Beyond catalysis, nickel also offers economic advantages. Moreover, nickel with loosely bound valence electrons represents a more cost-effective electrode material compared to platinum group metals. Of particular note, nickel-cobalt layered double hydroxide (NiCo-LDH) emerges as an electrocatalyst with distinctive advantages, demonstrating prominent performance in alkaline OER [27,28]. The polypyrrole (PPy) shell-core architecture creates synergistic effects by combining PPy's high conductivity and corrosion resistance with the metal oxide core's abundant

* Corresponding authors.
E-mail addresses: liyuca@163.com (Y. Li), miaolihua@163.com (L. Miao).
[1] These authors contributed equally to this work.

https://doi.org/10.1016/j.jelechem.2025.119759
Received 26 September 2025; Received in revised form 15 December 2025; Accepted 22 December 2025
Available online 30 December 2025

active sites, resulting in enhanced charge transfer and significantly reduced activation energy for water splitting reactions. For instance, in NiCo2O4@PPy, the PPy shell confers superior corrosion resistance (50 h stable operation), enabling an overpotential of 203 mV and a Tafel slope of 46 mV dec^{-1} at 10 mA cm^{-2} while optimizing OER kinetics [29]. Similarly, in ZnCo2O4@PPy-200, the PPy shell enhances conductivity (ECSA: 0.119 mF cm^{-2}) and corrosion resistance (42 h stability), translating to an overpotential of 254 mV and a Tafel slope of 60.77 mV dec^{-1} at the same current density, significantly lowering OER activation energy [30].

Thus, in the present study, NiCo-LDH materials were synthesised via a hydrothermal approach, and a series of NiCo-LDH@PPy nanowires were fabricated through electrochemical deposition. Electrochemical evaluations of OER and HER activities revealed that, within this series, NiCo-LDH@PPy-100 displayed superior electrocatalytic performance. Under alkaline electrolytic conditions at a current density of 50 mA cm^{-2}, the overpotential for the hydrogen evolution reaction (HER) was 210.7 mV, corresponding to a Tafel slope of 298.03 mV dec^{-1}. The overpotential for the OER was 360.2 mV, with a Tafel slope of 79.83 mV dec^{-1}. Notably, the material maintained excellent stability after 28 h of continuous cycling at a current density of 10 mA cm^{-2}. In an alkaline seawater electrolysis environment, at a current density of 50 mA cm^{-2}, the overpotential for hydrogen evolution was 223.7 mV and that for oxygen evolution was 270.1 mV. The material also exhibits excellent stability during 28 h of continuous cycling. Furthermore, the hydrothermal-electrodeposition synthesis of NiCo-LDH@PPy yields a high-specific-surface-area hierarchical structure, facilitating active site exposure and mass transfer processes. The electrocatalytic performance of NiCo-LDH@PPy-100 approaches that of precious metals such as iridium, while delivering robust overall water-splitting capabilities in seawater. This offers novel prospects for the large-scale industrial application of electrocatalytic technologies.

2. Experiment

2.1. Preparation of NiCo-LDH nanowires

Prior to the experimental synthesis of the material, four pieces of nickel foam (NF) measuring 4 × 4 cm^2 were immersed in a 1 M HCl solution for cleaning. Subsequently, the NF was rinsed multiple times sequentially with deionised water and ethanol. Finally, the treated sponge nickel was placed in an oven to dry for subsequent use. Material synthesis was then carried out using the following preparation method: First, 2 mmol $Ni(NO_3)_2{\cdot}6H_2O$ and 3 mmol $Co(NO_3){\cdot}6H_2O$ were added to 60 mL of deionised water and stirred until completely dissolved. Subsequently, 0.3 g of urea was added to the mixed solution and stirred for 30 min. Four identical samples were prepared using the same experimental method. Subsequently, the four pretreated NF samples (each measuring 4 × 4 cm^2) were transferred together with the aforementioned solution into a 100 mL autoclave. The autoclave was placed in an oven and heated at 120 °C for 5 h. After the reaction system had fully reacted, allow it to cool naturally to room temperature. Subsequently, wash the resulting precursor alternately with deionised water and anhydrous ethanol to remove impurity ions and residual reaction products. Finally, place the washed samples in a constant-temperature drying oven and dry at 60 °C for 12 h to obtain the dried NiCo-LDH nanomaterial product.

2.2. Synthesis of NiCo-LDH@PPy composite structures

The experiment employed electrochemical deposition to coat the material with polypyrrole (PPy). First, 1 mL of pyrrole solution and 4 g of p-benzenesulfonic acid were weighed and added to 100 mL of deionised water, then stirred magnetically until completely dissolved. The solution was subsequently transferred to a three-electrode cell to serve as the electrolyte for the coating reaction. The electrode system configuration was as follows: an Ag/AgCl electrode served as the reference electrode, a Pt electrode as the counter electrode, and a pre-prepared NiCo-LDH precursor as the working electrode. Electrochemical deposition of PPy was conducted using the constant voltage method on an electrochemical workstation. During the experiment, a constant voltage of 0.9 V was applied for deposition durations of 50 s, 100 s, and 200 s, respectively. Depending on the deposition duration, the resulting electrode discs were designated NiCo-LDH@PPy-50, NiCo-LDH@PPy-100, and NiCo-LDH@PPy-200, respectively. Finally, the samples underwent multiple rinses with deionised water and anhydrous ethanol before being dried in a 60 °C oven.

2.3. Structure characterization

The morphology and crystal structure of the prepared products were characterized using X-ray diffraction (XRD, Shimadzu-7000, Cu Kα radiation), X-ray photoelectron spectroscopy (XPS, ESCALAB 250 equipped with Al Kα source), Fourier transform infrared spectroscopy (FTIR, 4000–500 cm^{-1}), scanning electron microscopy (SEM, Gemini 300–71-31), and transmission electron microscopy (TEM, JEM-2100 PLUS).

2.4. Electrocatalytic characterization

The electrochemical performance of all electrocatalysts was evaluated using a CHI660E electrochemical workstation. Linear sweep voltammetry (LSV), cyclic voltammetry (CV), and chronoamperometry (CA) were measured in a three-electrode system employing electrolytes comprising 1 M KOH aqueous solution (pH = 13.7) and 1 M KOH seawater solution (pH = 13.5). For these tests, a 95 % compensation factor was applied to prevent potentiostat oscillations and minimize overcorrection artifacts, in line with standard practices recommended in the electrocatalysis literature. The synthesised samples served as the working electrode, with Ag/AgCl acting as the reference electrode. Platinum foil and graphite rod were employed as counter electrodes for the OER and HER, respectively. All potentials were converted to reversible hydrogen electrode (RHE) potentials via the Nernst equation $E_{RHE} = E_{Ag/AgCl} + 0.197 + 0.059 \times pH$, where $E_{Ag/AgCl}$ represents the experimentally measured potential relative to the Ag/AgCl reference electrode. Overpotential (η) was calculated using the following formula: $\eta = E_{RHE} - 1.23$. It should be noted that the catalyst loading was nominally controlled but not quantitatively determined; therefore, the electrocatalytic performance discussed in this work is intended for relative comparison among the studied samples rather than absolute benchmarking.

3. Results and discussion

Fig. 1a presents the XRD patterns of the prepared samples NiCo-LDH, NiCo-LDH@PPy-50, NiCo-LDH@PPy-100, and NiCo-LDH@PPy-200. Through these XRD patterns, the crystalline structures of the prepared samples can be observed. Strong diffraction peaks at 2θ values of 44.4°, 51.6°, and 76.1° correspond to the nickel foam. However, the magnified XRD pattern (Fig. 1b) allows for better observation of these peaks, which are less pronounced due to the significant influence of the nickel sponge substrate on the XRD measurement. The peaks at 2θ values of 15.6°, 26.2°, 28.7°, and 38.3° can be indexed to the (111), (204), (115), and (131) planes of the NiCo-LDH phase (JCPDS: 24–0523). (115) planes of the NiCo-LDH phase (JCPDS: 24–0523). Additional peaks at 2θ values of 23.2°, 34.1°, and 38.3° correspond to the (006), (012), and (015) crystal planes of the NiCo-LDH phase (JCPDS: 40–0216). Notably, diffraction peak intensity varies with PPy deposition time: NiCo-LDH@PPy-100 exhibits the highest intensity, suggesting improved crystalline ordering or signal transmission from uniform PPy encapsulation. In contrast, NiCo-LDH@PPy-50 shows lower intensity (likely due to incomplete coverage), while NiCo-LDH@PPy-200 shows no further intensity increase but a slight decrease—attributed to an overly thick or

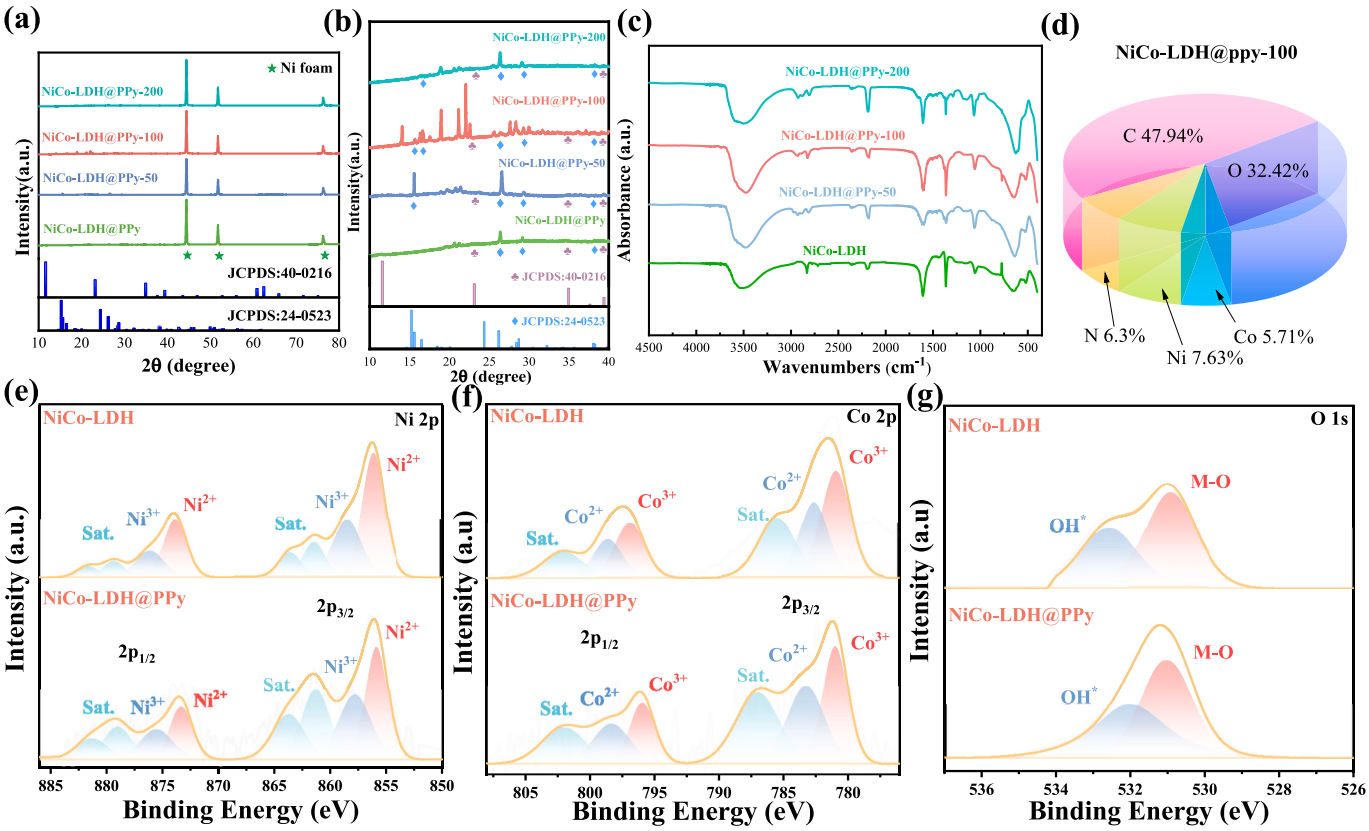

Fig. 1. Structure characterization of as-fabricated samples (a) XRD patterns (b) XRD 10–40° Enlarged View (c) FTIR profile (d) NiCo-LDH@PPy Elemental Ratios Pie Chart (e) XPS of Ni 2p (f) Co 2p (g) O 1 s.

disordered PPy layer that may attenuate LDH diffraction signals.

These results indicate an favourable PPy deposition time (100 s) that balances encapsulation and LDH crystallinity, which is crucial for preserving the material's catalytic activity.

To further validate the presence of PPy, FTIR spectroscopy was conducted, with results presented in Fig. 1c. Within the spectrum, the absorption peak at 3000 cm^{-1} corresponds to the stretching vibration of C—H bonds in the sample, whilst the peak at 1550 cm^{-1} is attributed to the stretching vibration of C═C bonds. Furthermore, absorption peaks at 2353 cm^{-1} and 2917 cm^{-1} are respectively assigned to N—H bond vibrations, whilst the peak at 1618 cm^{-1} originates from C═N bond stretching vibrations [31]. The presence of these characteristic peaks further confirms the successful coating of PPy onto the sample surface.

Beyond the characteristic peaks of PPy, the fingerprint region (800–1400 cm^{-1}) shows several absorption bands that likely correspond to δ(M-OH) bending vibrations and carbonate species. Particularly notable is the band around 1380 cm^{-1}, which appears consistent across samples and likely represents ν_3 vibration of intercalated CO_3^{2-} ions. The broad absorption features visible around 500–600 cm^{-1} correspond to M-O and M-O-M stretching vibrations (where M represents Ni or Co). These bands appear to maintain relatively consistent positions across all samples, suggesting the LDH layer structure remains intact after PPy coating.

Table 1
OER electrocatalytic performance of several electrode materials.

Materials	Overpotential (mV)	Tafel (mV dec^{-1})	Electrolyte	Ref.
NiCo-LDH/NF	391 (50 mA cm^{-2})	117	1.0 M KOH	[38]
FeCoNi-LTH/CC	386 (50 mA cm^{-2})	166	1.0 M KOH	[39]
P123-$NiCo_2O_4$	405 (25 mA cm^{-2})	109.88	1.0 M KOH	[40]
$Ni(OH)_2$	380 (50 mA cm^{-2})	123.4	1.0 M KOH	[41]
NiFe-LDH	390 (50 mA cm^{-2})	104	1.0 M KOH	[42]
NiCo-LDH	370.3 (50 mA cm^{-2})	100.65	1.0 M KOH	This work
NiCo-LDH@PPy-50	400.4 (50 mA cm^{-2})	115.71	1.0 M KOH	This work
NiCo-LDH@PPy-100	360.2 (50 mA cm^{-2})	79.83	1.0 M KOH	This work
NiCo-LDH@PPy-200	380.9 (50 mA cm^{-2})	109.74	1.0 M KOH	This work

Based on the aforementioned experimental results, we further employed XPS to analyse the chemical composition and valence states of the synthesised material. The elemental contents of Ni, Co, O, C, and N were determined to be 7.63 %, 5.71 %, 32.42 %, 47.94 %, and 6.3 % respectively, as shown in Fig. 1d. Fig. 1e displays the refined Ni 2p spectrum, clearly revealing Ni^{3+}, Ni^{2+}, and satellite peaks. In NiCo-LDH@PPy-100, the characteristic peaks of Ni^{2+} in the Ni 2p orbital region exhibit typical spin-orbit splitting, with the two characteristic peaks of Ni $2p_{3/2}$ and Ni $2p_{1/2}$ located at binding energies of 855.7 eV and 873.3 eV, respectively, which may originate from the formation of nickel oxide through the bonding between Ni and O elements [32]; the spin-orbit splitting of Ni^{3+} in the Ni $2p_{3/2}$ and Ni $2p_{1/2}$ orbitals is primarily positioned at 857.8 eV and 875.6 eV, which may result from the formation of Ni—C compound phases [33–35]. Compared to NiCo-LDH, the Ni^{3+} peak in NiCo-LDH@PPy-100 exhibits a positive shift due to electron density transfer from NiCo-LDH to PPy, confirming interfacial electronic interactions. In NiCo-LDH@PPy-100, the four split peaks at 861.4 eV, 863.8 eV, 879.0 eV, and 881.2 eV represent satellite peaks of Ni. Fig. 1f presents the Co 2P fine spectrum. It displays two diffraction peaks from Co $2p_{1/2}$ and Co $2p_{2/3}$, alongside two satellite peaks arising from spin-orbit coupling between Co $2p_{1/2}$ and Co $2p_{3/2}$ orbitals. In NiCo-LDH@PPy-100, the diffraction peaks originating from the Co $2P_{3/2}$ orbital are predominantly centred at binding energies of 780.9 eV and 783.3 eV, corresponding to Co^{3+} and Co^{2+}, respectively. Similarly, the

peaks from the Co $2P_{1/2}$ orbital are concentrated at 795.9 eV and 798.4 eV, also attributed to Co^{3+} and Co^{2+}. These binding energy peaks likely originate from the formation of oxides through the bonding of Co and O elements, where both the divalent and trivalent states of Co may coexist within the oxides [36]. Furthermore, the split peaks at 787.1 eV and 802.2 eV are attributed to satellite peaks of Co. Relative to NiCo-LDH, NiCo-LDH@PPy exhibits a positive shift in Co 2p binding energy, indicating that the PPy coating withdraws electron density from the cobalt centers and modulates the electronic structure through interfacial charge transfer, thereby enhancing the electrochemical activity of the material. Fig. 1g presents the O 1 s fine spectrum. In NiCo-LDH@PPy-100, the O 1 s diffraction peak is resolved into two peaks at 531.0 eV and 532.0 eV, corresponding to the metal-oxygen (M-O) and hydroxide groups, respectively [37]. The O 1 s spectrum of NiCo-LDH@PPy shows a positive shift in binding energy for the M-O peaks, demonstrating that the PPy coating induces electron redistribution at the oxygen sites, which strengthens the metal-oxygen interactions.

The microstructure of the synthesised samples was investigated by characterising the materials using SEM. TEM was employed to observe and analyse high-resolution regions of the nanomaterials and their interplanar spacings, as illustrated in Fig. 2. The pristine NiCo-LDH sample (Figures a, b) displays densely packed nanowires with diameters of several tens of nanometers. The open interwire spacing creates a porous network that facilitates electrolyte penetration and exposes numerous electrochemically active sites. Following 50 s of PPy deposition, the NiCo-LDH@PPy-50 composite (Figures c, d) retains the nanowire morphology with sparse polymer coating. The discontinuous coverage indicates insufficient polymer network formation, which limits electronic conductivity enhancement. The NiCo-LDH@PPy-100 sample (Figures e, f) exhibits a uniform PPy coating that conformally covers the substrate while preserving the inherent porosity. This moderate coating thickness enables effective electron transport while maintaining accessibility to active sites and open channels for ion diffusion, achieving a favourable balance between conductivity and electrochemical accessibility. The NiCo-LDH@PPy-200 sample (Figures g, h) exhibits densely packed nanowires with a thick PPy coating. Although electronic conductivity is improved, the excessive accumulation of PPy obscures the original nanostructure, reducing the effective surface area and hindering ion transport. Fig. 2i and j show the TEM images of NiCo-LDH@PPy-100 at different magnifications. In Fig. 2i (low magnification, 100 nm scale

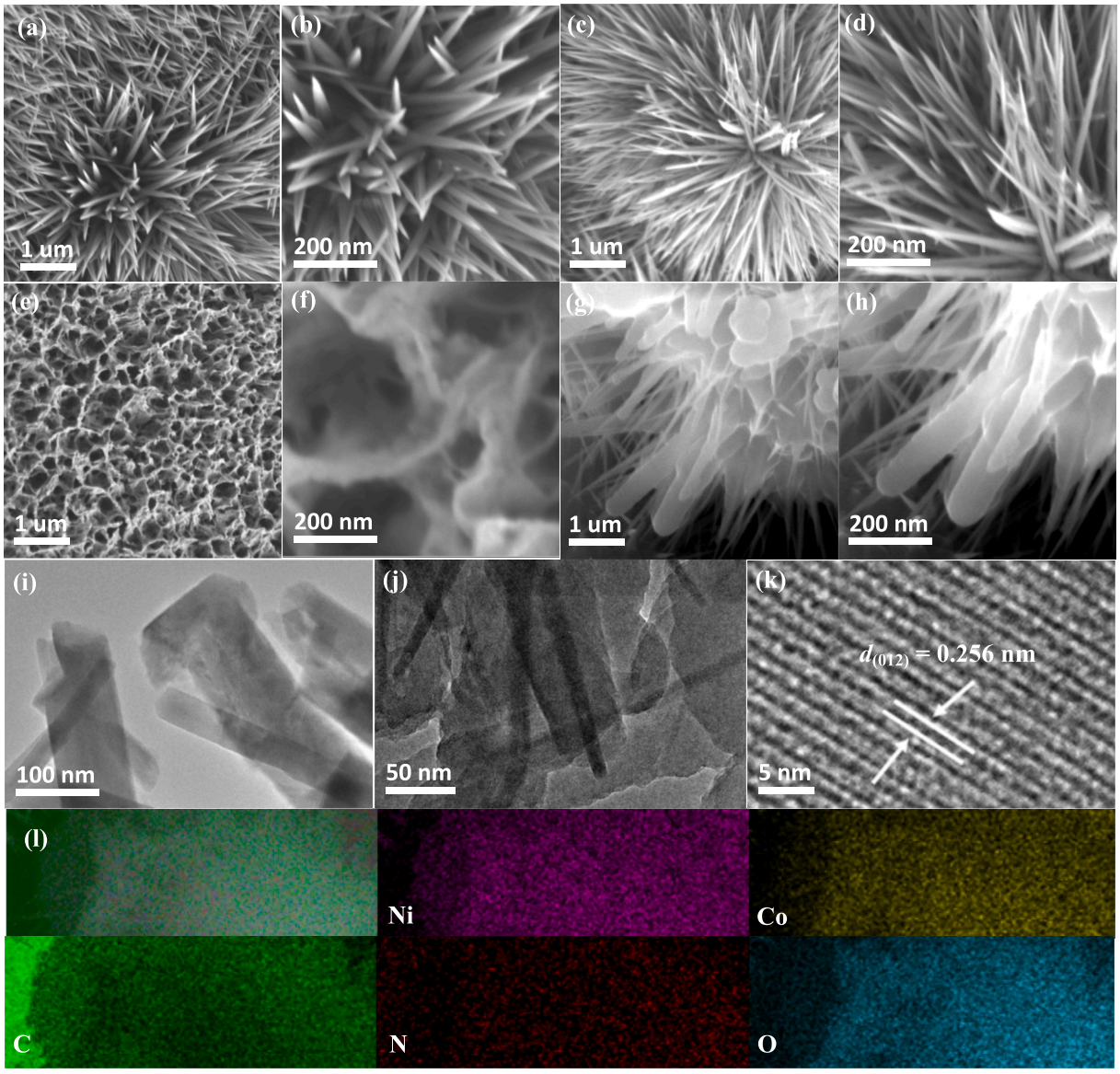

Fig. 2. Morphology and structure characterization of the as-prepared products (a, b) SEM images of NiCo-LDH (c, d) SEM images of NiCo-LDH@PPy-50 (e, f) SEM images of NiCo-LDH@PPy-100 (g, h) SEM images of NiCo-LDH@PPy-200 (i-k) TEM images of NiCo-LDH@PPy (l) EDS mapping NiCo-LDH@PPy.

bar), the nanorod-like morphology of NiCo-LDH@PPy-100 is observed. Fig. 2j (higher magnification, 50 nm scale bar) further demonstrates that these nanorods are uniformly coated with a thin layer of conductive PPy, verifying the successful encapsulation of PPy on NiCo-LDH. The HRTEM image in Fig. 2k clearly demonstrates the highly crystalline, plate-like nanostructure of the material, with well-defined crystalline striations readily observable. Measurement of the lattice spacing yields a value of 0.256 nm. Cross-referencing with the XRD analysis reveals correspondence to the (012) crystal plane displayed in the XRD pattern, confirming the successful synthesis of NiCo-LDH@PPy. Fig. 2l presents the elemental mapping analysis of the sample. This reveals the distribution of constituent elements within the material, with distinct colours assigned to different elements. Ni, Co, O, C, and N elements are uniformly distributed throughout the region. This further validates the successful synthesis of the precursor material and the effective encapsulation of PPy.

To evaluate the HER activity variations of the synthesised materials, a 1 M KOH solution was employed as the alkaline electrolyte. A series of electrochemical performance tests was conducted using a three-electrode system, with the experimental results presented in Fig. 3. Fig. 3a demonstrates that at a current density of 50 mA cm^{-2}, the noble metal material Pt/C exhibits an overpotential of 87.4 mV, while the NiCo-LDH@PPy-100 sample shows an overpotential of 210.7 mV. This value is significantly lower than those of NiCo-LDH (220.7 mV), NiCo-LDH@PPy-50 (237.7 mV), and NiCo-LDH@PPy-200 (224.7 mV). The lower overpotential reduces the additional energy input required for the reaction, thereby substantially decreasing operational energy consumption. Fig. 3b displays the overpotentials corresponding to the LSV curves. NiCo-LDH@PPy-100 exhibits the lowest overpotential at both 50 mA cm^{-2} and 100 mA cm^{-2}, demonstrating its superior electrocatalytic performance. Fig. 3c presents the Tafel plots derived from the polarization curves recorded at 1 mV/s with iR compensation. The Tafel slopes were determined across 50–80 mA/cm^2 where the observed values reflect the combined contributions of charge transfer kinetics, mass transport limitations, and ohmic resistance characteristic of high current density operation. The NiCo-LDH@PPy-100 sample exhibits a Tafel slope of 175.81 mV dec^{-1}, compared to 264.95 mV dec^{-1} for NiCo-LDH, 298.01 mV dec^{-1} for NiCo-LDH@PPy-50, and 216.05 mV dec^{-1} for NiCo-LDH@PPy-200. While Tafel slopes provide insight into reaction kinetics and mechanisms, they do not serve as direct indicators of catalytic activity. The superior electrocatalytic performance of NiCo-LDH@PPy-100 is primarily established through its lower overpotential requirements at defined current densities (Fig. 3a and b), which represents the most reliable metric for assessing HER activity. Fig. 3d summarizes the double-layer capacitance (C_{dl}) of the samples. NiCo-LDH@PPy-100 exhibits the highest C_{dl} (0.013 mF cm^{-2}), compared with NiCo-LDH (0.010 mF cm^{-2}), NiCo-LDH@PPy-50 (0.008 mF cm^{-2}), and NiCo-LDH@PPy-200 (0.009 mF cm^{-2}). Accordingly, NiCo-LDH@PPy-100 is expected to provide the largest ECSA estimated from C_{dl}. This trend is consistent with a moderate, conformal PPy deposition that improves electronic pathways while largely preserving the porous framework and exposure of electrochemically active sites. In contrast, PPy over-deposition in NiCo-LDH@PPy-200 may partially fill inter-wire voids and reduce electrolyte accessibility, leading to a lower apparent ECSA. Overall, these results highlight that the PPy deposition level plays a key role in balancing electronic conductivity and electrochemical accessibility.

A series of electrochemical testing methods was employed to systematically characterize the OER catalytic activity of the samples, with the corresponding polarization curves shown in Fig. 4.

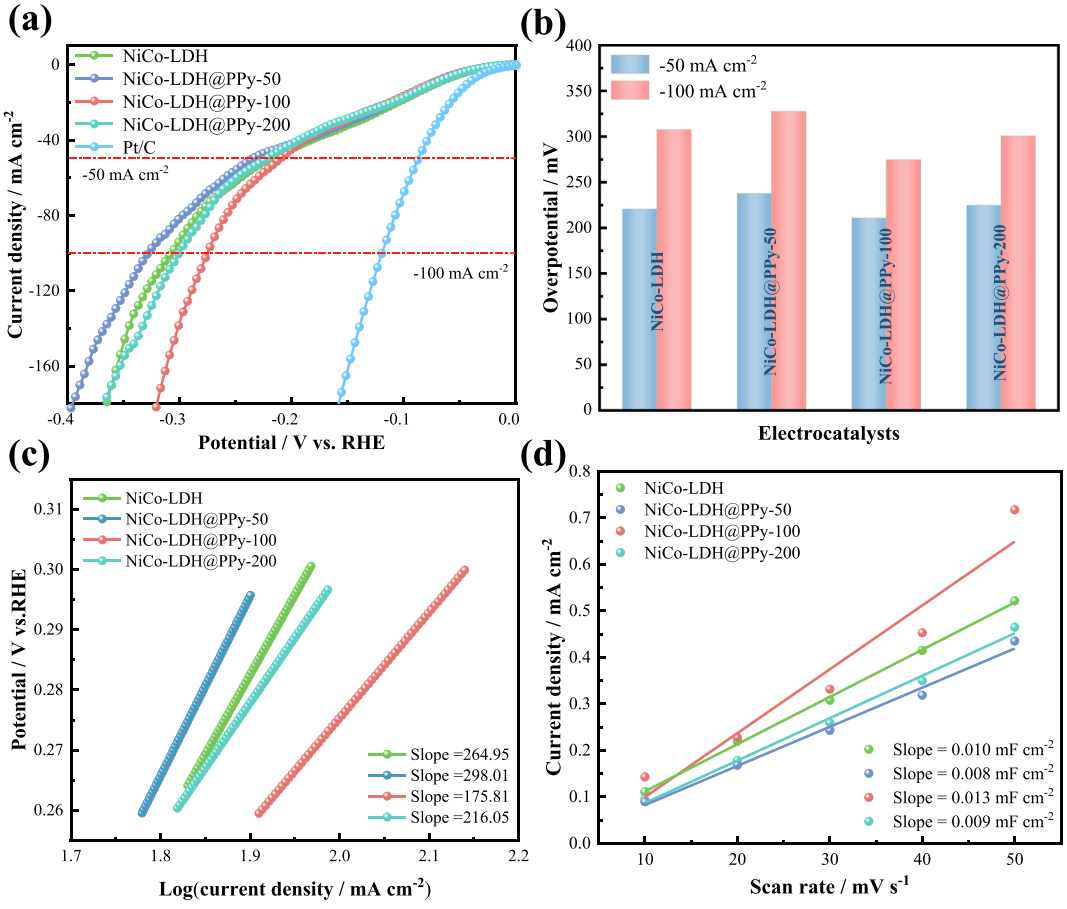

Fig. 3. HER properties of NiCo-LDH@PPy in 1 M KOH (a) LSV curves (b) overpotential for HER (c) Tafel plots (d) double-layer capacitance (C_{dl}).

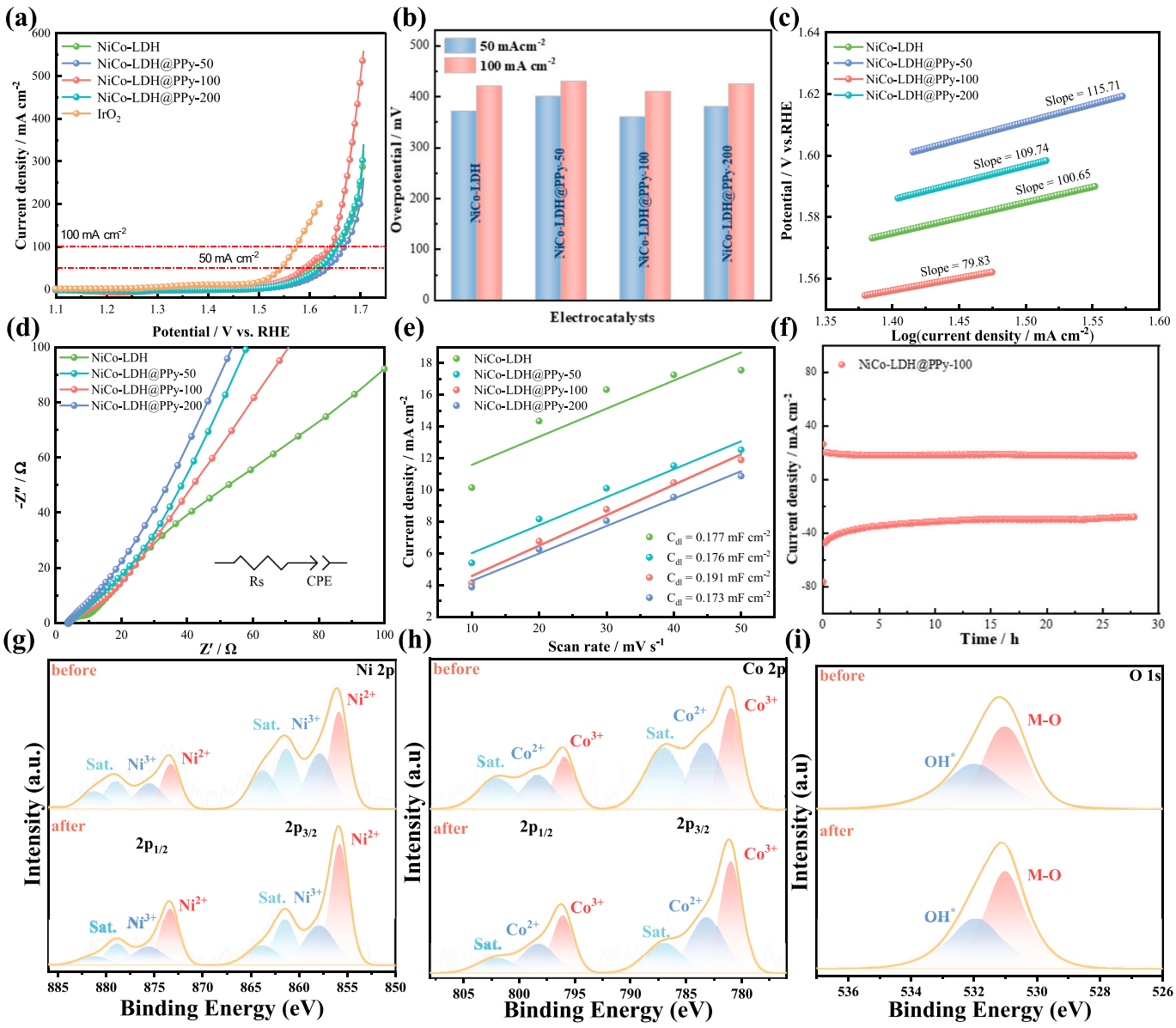

Fig. 4. OER properties of NiCo-LDH@PPy in 1 mol/L KOH (a) LSV curves (b) overpotential for OER (c) Tafel plots (d) EIS curves (e) double-layer capacitance (C_{dl}) (f) chronoamperometric stability tests of NiCo-LDH@PPy-100 (g) Before and after cycling: Comparative XPS spectra of Ni 2p (h) Co 2p (i) O 1 s.

Fig. 4a presents the LSV curves of the prepared samples under oxygen evolution conditions. It can be observed that at a current density of 50 mA cm^{-2}, the noble metal oxide IrO_2 exhibits an overpotential of 330.4 mV, while NiCo-LDH@PPy-100 demonstrates an overpotential of 360.2 mV, which is lower than that of NiCo-LDH (370.3 mV), NiCo-LDH@PPy-50 (400.4 mV), and NiCo-LDH@PPy-200 (380.9 mV). As expected, NiCo-LDH@PPy-100 exhibits superior catalytic performance compared to the other three materials. (See Table 1) Fig. 4b displays the overpotentials of the four samples at current densities of 50 mA cm^{-2} and 100 mA cm^{-2}. Through comparative analysis, it can be clearly observed that NiCo-LDH@PPy-100 consistently exhibits the lowest overpotential under different current density conditions. This characteristic fully confirms that its OER performance is superior to that of the other three comparative materials. The Tafel plots derived from the polarization curves were analyzed to evaluate OER kinetics (Fig. 4c). The NiCo-LDH@PPy-100 sample exhibits a Tafel slope of 79.83 mV dec^{-1}, which is lower than those of NiCo-LDH (100.65 mV dec^{-1}), NiCo-LDH@PPy-50 (115.71 mV dec^{-1}), and NiCo-LDH@PPy-200 (109.74 mV dec^{-1}). These results suggest that the introduction of PPy (with excellent conductivity) may facilitate electron transfer to the electrode surface, thereby improving the catalytic reaction kinetics. To investigate the impedance characteristics of the samples, electrochemical impedance spectroscopy (EIS) measurements were performed on the prepared materials to study their kinetic performance under alkaline conditions, as shown in Fig. 4d. Due to the absence of a resolvable semicircle in the Nyquist plots, the impedance spectra obtained in 1 M KOH were fitted using a simple series R_s-CPE model, since a reliable charge-transfer resistance could not be extracted under these conditions. As summarized in Table 2, NiCo-LDH@PPy-100 exhibits the lowest series resistance (R_s = 3.398 Ω), indicating reduced ohmic loss, which is consistent

Table 2
Fitted Rs-CPE impedance parameters of the electrodes in 1 M KOH.

Materials	Rs / Ω	CPE-T (Q)	CPE-P (n)	C_{eff}(1 Hz) / F·cm^{-2}
NiCo-LDH	4.006	0.0100	0.452	0.01461
NiCo-LDH@PPy-50	3.56	0.00341	0.552	0.00599
NiCo-LDH@PPy-100	3.398	0.00439	0.489	0.00687
NiCo-LDH@PPy-200	3.689	0.00237	0.611	0.00464

with its lowest OER overpotential. NiCo-LDH and NiCo-LDH@PPy-200 show comparable OER overpotentials despite different R_s values (4.006 and 3.689 Ω, respectively), which can be rationalized by their relatively higher interfacial polarization contributions compared with NiCo-LDH@PPy-50. In contrast, NiCo-LDH@PPy-50, although exhibiting a moderate R_s (3.56 Ω), presents a reduced interfacial capacitance and increased non-ideality, suggesting limited interfacial accessibility, which correlates with its inferior OER activity. Overall, the R_s-CPE fitting parameters qualitatively reflect the combined influence of ohmic resistance and non-ideal interfacial polarization on the observed OER activity trend. As shown in Fig. 4e, NiCo-LDH@PPy-100 delivers the highest C_{dl} (0.191 mF cm^{-2}), compared with NiCo-LDH (0.177 mF cm^{-2}), NiCo-LDH@PPy-50 (0.176 mF cm^{-2}), and NiCo-LDH@PPy-200 (0.173 mF cm^{-2}). Accordingly, NiCo-LDH@PPy-100 exhibits the largest ECSA, as estimated from C_{dl}. This improvement is attributed to a moderate, conformal PPy coating that preserves the inter-nanowire porosity, thereby maintaining open channels for electrolyte infiltration and ion transport while facilitating electron transfer. In contrast, insufficient PPy coverage (PPy-50) provides limited conductivity enhancement, whereas over-deposition (PPy-200) tends to partially block interstitial voids and reduce electrolyte accessibility, leading to a lower apparent ECSA. The sample material NiCo-LDH@PPy-100 underwent cyclic stability testing for hydrogen evolution and oxygen evolution reactions over a period of 28 h, as depicted in Fig. 4f. It demonstrated reliable electrochemical stability with no discernible current fluctuations.

Subsequently, the cycled NiCo-LDH@PPy-100 material was subjected to XPS to analyse the chemical composition and valence states of the synthesised material. Fig. 4g presents the refined Ni 2p spectrum, where the splitting gap between the Ni^{2+} spin orbitals Ni $2p_{3/2}$ and Ni $2p_{1/2}$ primarily occurs at 855.7 eV and 873.3 eV. For Ni^{3+}, the splitting gaps in the Ni $2p_{3/2}$ and Ni $2p_{1/2}$ spin orbitals are primarily located at 857.9 eV and 875.6 eV. The four splitting peaks at 861.4 eV, 863.8 eV, 878.8 eV, and 881.2 eV correspond to satellite peaks of Ni. Fig. 4h presents the Co 2p fine spectrum. It displays two diffraction peaks corresponding to Co $2p_{1/2}$ and Co $2p_{2/3}$, alongside two satellite peaks arising from spin-orbit coupling between the Co $2p_{1/2}$ and Co $2p_{3/2}$ orbitals. The diffraction peaks originating from the Co $2P_{3/2}$ orbital are predominantly centred at binding energies of 780.9 eV and 783.3 eV, corresponding to Co^{3+} and Co^{2+}, respectively. Similarly, the peaks from the Co $2P_{1/2}$ orbital are concentrated at 796.2 eV and 798.3 eV, also attributed to Co^{3+} and Co^{2+}. The split peaks at 787.1 eV and 802.2 eV are attributed to satellite peaks of Co. Fig. 4i presents the O 1 s fine spectrum. The O 1 s diffraction peaks are resolved into two peaks at 531.0 eV and 531.9 eV, corresponding to the M-O and hydroxide groups, respectively. Comparison reveals minimal shifts in the XPS peak positions. This indicates that the presence of PPy prevents significant surface binding energy shifts during oxygen evolution cycles in NiCo-LDH, maintaining its chemical bonding state and structural stability, thereby demonstrating robust chemical stability.

As shown in Fig. 5, given the excellent OER and HER catalytic activities of the NiCo-LDH@PPy-100 sample, its overall water splitting performance was investigated using a simple two-electrode configuration in a regular electrolytic cell with 1 M KOH. Specifically, the widely accepted benchmark of 10 mA cm^{-2} was adopted for overall water splitting, while 50 mA cm^{-2} was used for individual HER and OER to better assess performance under practical conditions. Based on the data presented in Fig. 5a, it can be clearly observed that the NiCo-LDH@PPy-100 material demonstrates relatively better performance. At a current density of 10 mA cm^{-2}, the cell voltage of NiCo-LDH@PPy-100 is 1.61 V,

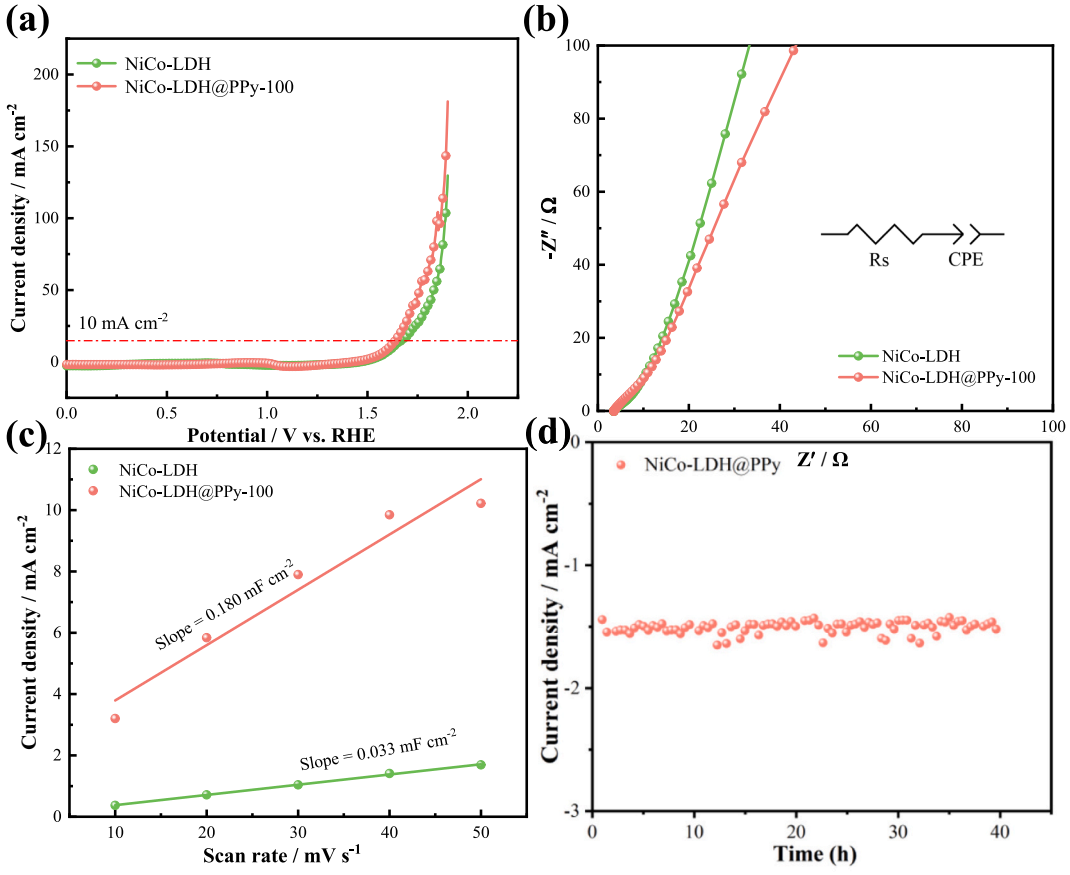

Fig. 5. Total hydrolysis properties of NiCo-LDH@PPy in 1 mol/L KOH (a) LSV curves (b) EIS curves (c) double-layer capacitance (C_{dl}) (d) chronoamperometry stability tests of NiCo-LDH@PPy-100.

which is lower than that of NiCo-LDH (1.63 V). Fig. 5b presents the impedance spectra of the synthesised materials. In 1 M KOH overall water splitting, both electrodes show quasi-linear Nyquist responses without a resolved semicircle and were fitted using a series Rs–CPE model. NiCo-LDH@PPy-100 exhibits a lower series resistance (R_s = 3.62 Ω) than NiCo-LDH (R_s = 3.82 Ω), while the similar n values (0.66–0.67) indicate non-ideal interfacial polarization dominated impedance behavior under gas evolution. Fig. 5c presents the CV test results for the material. It can be observed that the C_{dl} value of NiCo-LDH@PPy-100 is 0.180 mF cm^{-2}, which is greater than that of NiCo-LDH (0.033 mF cm^{-2}). This indicates that NiCo-LDH@PPy-100 possesses a larger ECSA and more reactive sites. Finally, full water-splitting stability testing was conducted, as shown in Fig. 5d. The chronoamperometry stability test of the NiCo-LDH@PPy-100 electrode was performed in 1 M KOH aqueous electrolyte at a cell voltage of 1.65 V. After 40 h, the current density remained essentially unchanged, indicating satisfactory stability for water splitting.

In summary, the four materials were fabricated via a straightforward method on nickel foam. The deposition time of PPy significantly influences the catalytic performance of the electrode. The NiCo-LDH@PPy-100 sample exhibits superior OER and HER performance, featuring low overpotentials and notable durability. Concurrently, the water electrolysis cell demonstrates superior functionality, primarily benefiting from the unique structure and synergistic effects between NiCo-LDH and PPy materials. The incorporation of PPy enhances electrode conductivity and facilitates efficient electron transfer during both OER and HER.

To evaluate the variation in HER performance of the synthesised materials under different environments, the electrocatalytic properties of the four samples were subsequently investigated in seawater solutions, as depicted in Fig. 6. Fig. 6a displays the IR-corrected LSV polarization curves for these samples. The NiCo-LDH@PPy-100 sample, with a PPy deposition time of 100 s, exhibits relatively more active performance, featuring a minimum overpotential of 223.7 mV at a current density of 50 mA cm^{-2}. This performance surpassed that of NiCo-LDH (281.7 mV) and NiCo-LDH@PPy-50 (309.7 mV), and NiCo-LDH@PPy-200 (275.7 mV). Fig. 6b presents the overpotentials of the four materials at current densities of 50 mA cm^{-2} and 100 mA cm^{-2}. The figure clearly demonstrates that NiCo-LDH@PPy-100 exhibits the lowest overpotential compared to the other three materials. This enhancement is primarily attributed to the conductive PPy effectively improves the electronic conductivity of NiCo-LDH. Concurrently, the moderately thick PPy coating layer optimizes interfacial ion transport kinetics between the electrolyte and NiCo-LDH, thereby substantially enhancing the overall electrochemical performance. Subsequently, we analyzed the Tafel plots to evaluate the HER reaction kinetics (Fig. 6c). NiCo-LDH@PPy-100 exhibits the smallest Tafel slope of 110.35 mV dec^{-1}, which is lower than those of the other samples: NiCo-LDH (111.12 mV dec^{-1}), NiCo-LDH@PPy-50 (128.63 mV dec^{-1}), and NiCo-LDH@PPy-200 (118.17 mV dec^{-1}). Collectively, the reduced Tafel slope of NiCo-LDH@PPy-100, combined with its relatively lower overpotential, underscores that PPy modification enhances charge transfer kinetics, thereby synergistically contributing to comparatively better HER performance. Fig. 6d presents the C_{dl} values of the materials. The NiCo-LDH@PPy-100 electrocatalyst exhibits a C_{dl} value of 0.053 mF cm^{-2}, which exceeds those of NiCo-LDH (0.007 mF cm^{-2}), NiCo-LDH@PPy-50 (0.003 mF cm^{-2}), and NiCo-LDH@PPy-200 (0.004 mF cm^{-2}). The experimental results demonstrate that the NiCo-LDH@PPy-100 electrocatalyst possesses the largest reactive surface area. The ECSA exhibits a positive correlation with the number of exposed active sites, and

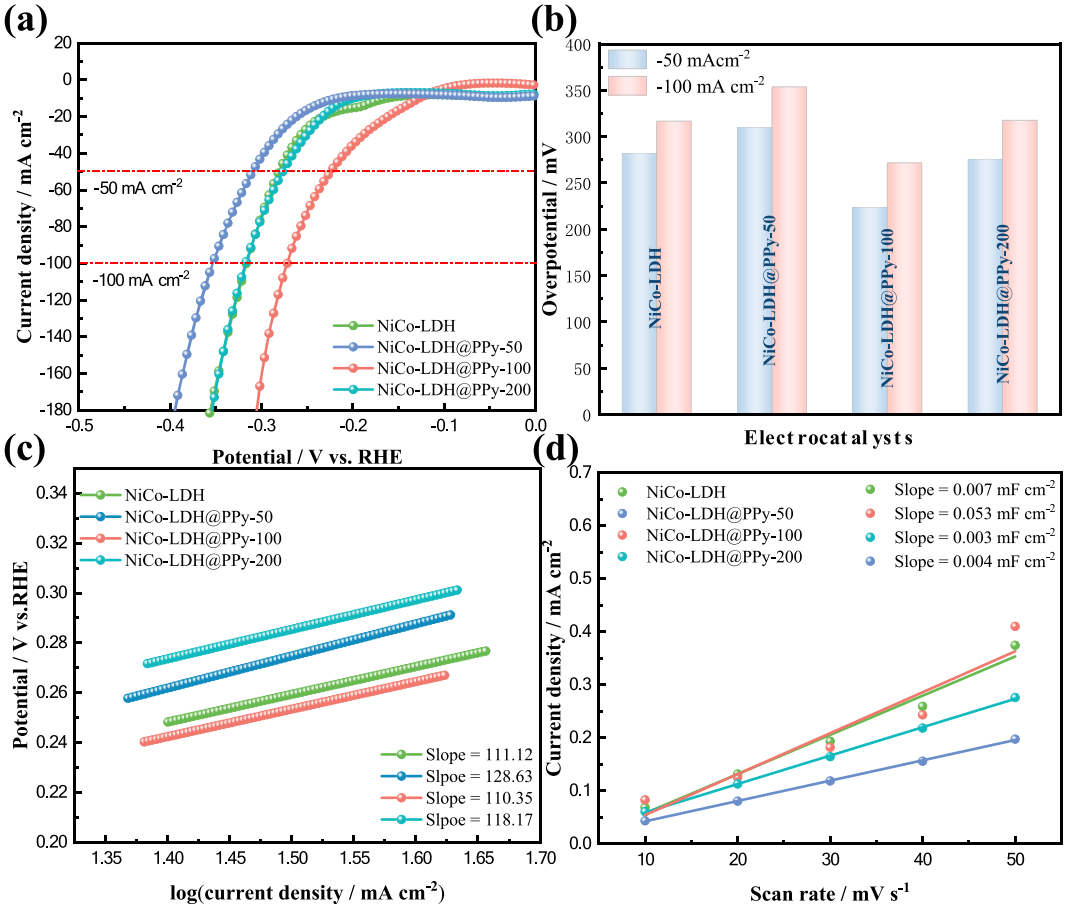

Fig. 6. HER properties of NiCo-LDH@PPy in seawater (a) LSV curves (b) overpotential for HER (c) Tafel plots (d) double-layer capacitance (C_{dl}).

higher ECSA values are beneficial for promoting electrocatalytic reactions. This finding confirms that by regulating the thickness of the PPy shell layer, the electrocatalytic activity of electrode materials can be effectively modulated, providing an important pathway for optimizing electrode performance.

To evaluate the catalytic performance of the material in practical application environments, this study employed multiple electrochemical experiments to systematically characterize its OER properties in seawater electrolyte, with results presented in Fig. 7. Fig. 7a displays the OER polarization curves for NiCo-LDH@PPy samples loaded with varying amounts of PPy over time. NiCo-LDH@PPy-100 exhibits improved OER performance compared to other samples, demonstrating a minimum overpotential of 270.1 mV at a current density of 50 mA cm^{-2}. This performance markedly surpasses that of the other samples: NiCo-LDH (300.2 mV), NiCo-LDH@PPy-50 (311.3 mV), and NiCo-LDH@PPy-200 (317.3 mV). Fig. 7b presents the overpotentials of the prepared samples at different current densities. The material deposited with PPy for 100 s exhibits the lowest overpotential and the most favourable OER activity across all current densities. Subsequently, Tafel plots were analyzed to investigate the OER kinetic mechanism (Fig. 7c). The Tafel slopes for NiCo-LDH, NiCo-LDH@PPy-50, NiCo-LDH@PPy-100, and NiCo-LDH@PPy-200 were found to be 54.26, 52.52, 47.53, and 55.91 mV dec^{-1}, respectively. The smallest Tafel slope of NiCo-LDH@PPy-100 indicated more favourable OER charge transfer kinetics. Furthermore, EIS was conducted to investigate the interfacial reaction kinetics and electron transfer characteristics of the catalysts. As depicted in Fig. 7d, in the seawater electrolyte, the impedance spectra were fitted using a series R_s-CPE model due to the absence of a resolvable semicircle. As summarized in Table 3, NiCo-LDH@PPy-100 exhibits the lowest series resistance (R_s = 3.47 Ω), which is consistent with its lowest OER overpotential. NiCo-LDH@NiCo-LDH and NiCo-LDH@PPy-50 show comparable OER activities despite different R_s values (3.54 and 3.52 Ω, respectively), indicating a trade-off between ohmic resistance and interfacial polarization. In contrast, NiCo-LDH@PPy-200 presents the largest R_s (3.59 Ω) together with a relatively reduced effective interfacial capacitance, suggesting constrained interfacial accessibility and correlating with its inferior OER performance in seawater. Fig. 7e presents the CV curves for the samples, with the ECSA of the prepared samples in the OER calculated using the same HER method. The C_{dl} value of NiCo-LDH@PPy-100 was 0.390 mF cm^{-2}, whereas those of NiCo-LDH, NiCo-LDH@PPy-50, and NiCo-LDH@PPy-200 were 0.260 mF cm^{-2}, 0.157 mF cm^{-2}, and 0.308 mF cm^{-2}, respectively, indicating that the synergistic interaction between NiCo-LDH and PPy resulted in low overpotentials and enhanced electrocatalytic performance. Fig. 7f displays the HER and OER durability of the four samples under seawater conditions. During the 28-h test, the NiCo-LDH@PPy-100 electrocatalyst showed notable stability across current densities from 10 to 100 mA cm^{-2}. It thus demonstrates strong structural and electrochemical stability for OER. The protective PPy shell also grants it favourable OER durability in seawater solutions.

Table 3
Fitted Rs-CPE impedance parameters of the electrodes in seawater.

Materials	Rs / Ω	CPE-T (Q)	CPE-P (n)	C_{eff}(1 Hz) / F·cm^{-2}
NiCo-LDH	3.54	0.0061	0.47	0.0148
NiCo-LDH@PPy-50	3.52	0.00049	0.78	0.00241
NiCo-LDH@PPy-100	3.47	0.0027	0.53	0.00405
NiCo-LDH@PPy-200	3.59	0.0016	0.59	0.00316

To comprehensively evaluate the bifunctional catalytic performance of the prepared materials, their HER and OER catalytic activities in seawater splitting reactions were further investigated, with the corresponding overall water splitting performance shown in Fig. 8. Fig. 8a presents the LSV polarization curves of the samples, demonstrating excellent overall water splitting performance at a current density of 10 mA cm^{-2}. The cell voltage of NiCo-LDH@PPy-100 is 1.64 V, which is lower than that of the NiCo-LDH sample (1.69 V). Fig. 8b displays the EIS measurements of the samples. In seawater overall water splitting, the Nyquist plots of both electrodes exhibit quasi-linear responses

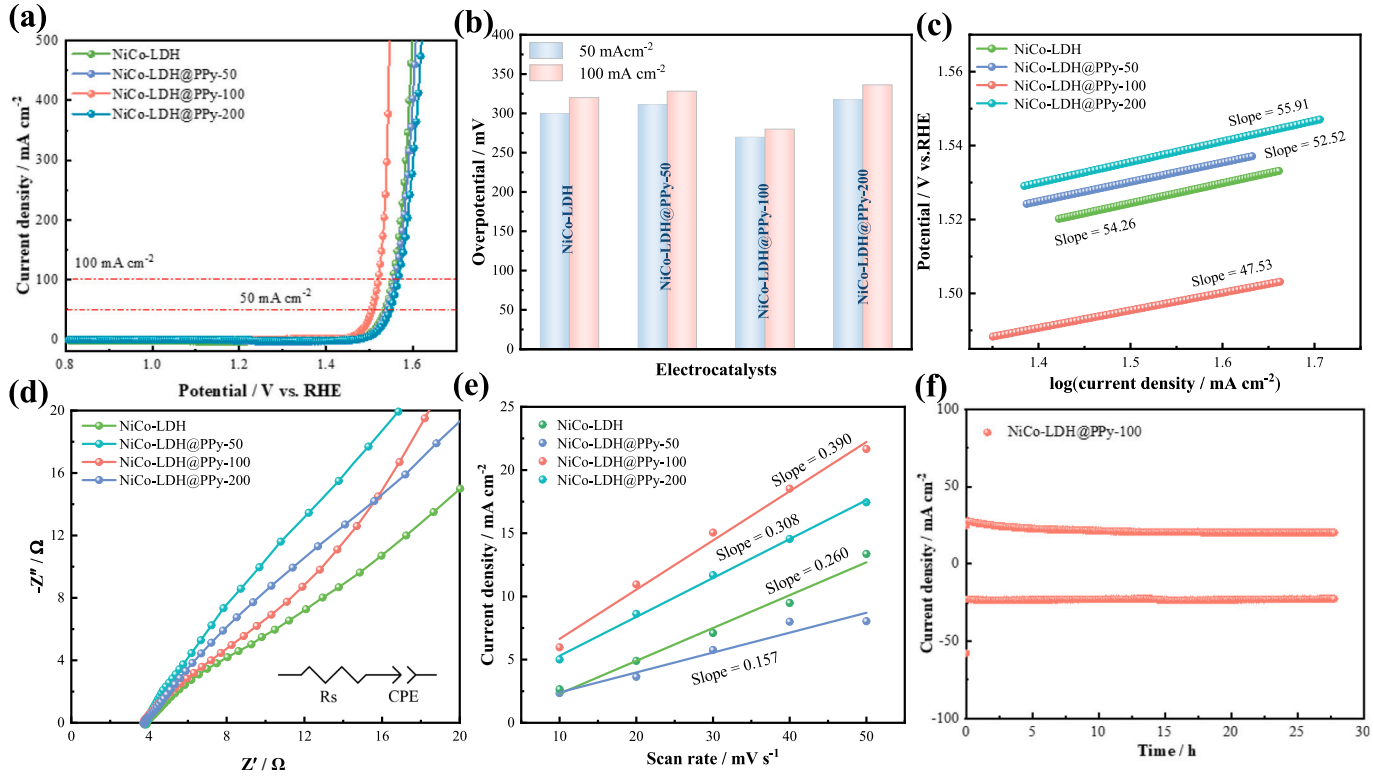

Fig. 7. OER properties of NiCo-LDH@PPy in seawater (a) LSV curves (b) overpotential for OER (c) Tafel plots (d) EIS curves (e) double-layer capacitance (C_{dl}) (f) chronoamperometric stability tests of NiCo-LDH@PPy-100.

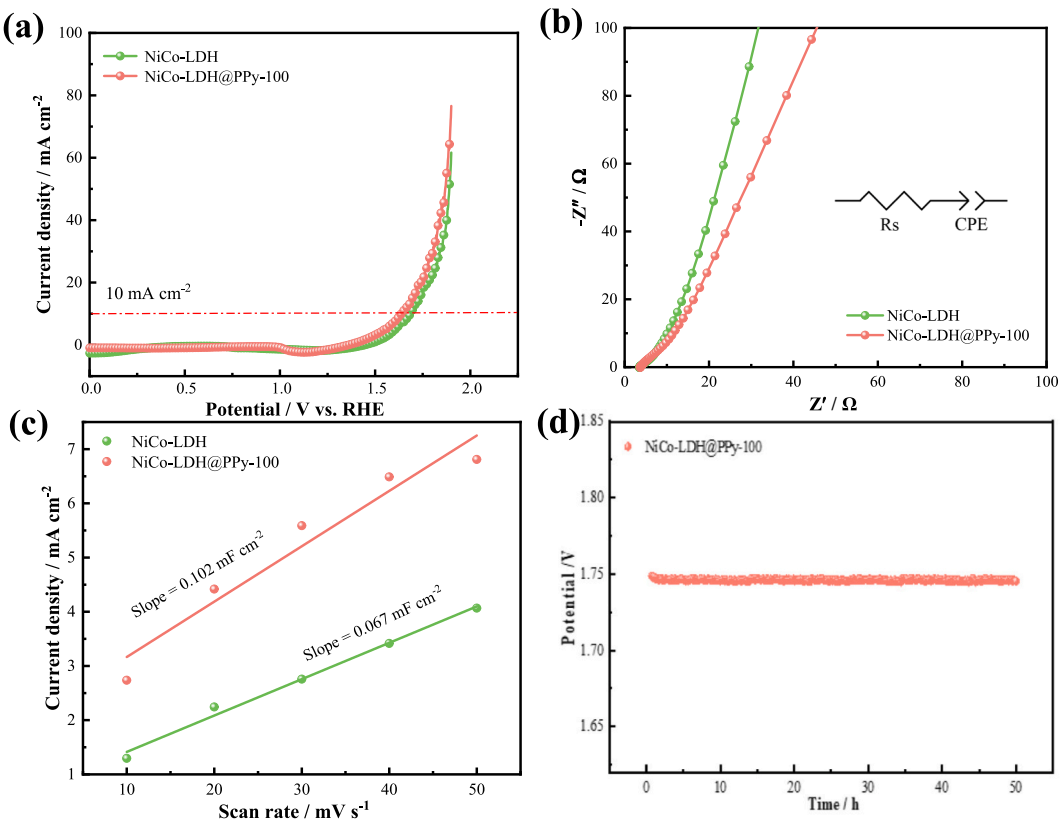

Fig. 8. Total hydrolysis properties of NiCo-LDH@PPy in seawater (a) LSV curves (b) EIS curves (c) double-layer capacitance (C_{dl}) (d) chronopotentiometry stability tests of NiCo-LDH@PPy-100.

without a resolvable semicircle; therefore, the impedance spectra were fitted using a series R_s-CPE model. NiCo-LDH@PPy-100 shows a slightly lower series resistance (R_s = 3.61 Ω) than NiCo-LDH (R_s = 3.69 Ω), indicating reduced ohmic loss in the full cell. Meanwhile, the n values for both electrodes (0.57–0.60) deviate significantly from unity, suggesting that the impedance response is dominated by non-ideal interfacial polarization and transport effects under vigorous gas evolution. Overall, the lower Rs of NiCo-LDH@PPy-100 contributes to its improved performance in seawater overall water splitting. Fig. 8c presents the C_{dl} values of the catalysts, revealing that the NiCo-LDH@PPy-100 sample exhibits a C_{dl} value of 0.180 mF cm^{-2}, which is greater than that of the NiCo-LDH sample (0.033 mF cm^{-2}), indicating relatively more active behavior. The practical application performance of the materials was evaluated through overall seawater splitting stability testing (Fig. 8d), with results demonstrating that NiCo-LDH@PPy-100 exhibits robust electrochemical stability during 50 h of continuous testing.

The substantial enhancement in material stability originates from the following mechanisms: The PPy protective layer serves dual functions, both suppressing the dissolution and loss of active components while constructing an efficient charge transport network. The surface reconstruction process induced by in situ electrochemical activation significantly increases the density of active sites. The synergistic effect between the PPy modification layer and surface reconstruction not only optimizes the electronic structure of the material but also enhances its durability under harsh seawater electrolysis conditions, thereby achieving simultaneous improvement in both HER and OER catalytic performance.

4. Conclusion

In response to the limitation of poor industrial-scale hydrogen production performance exhibited by NiCo-LDH, a core-shell structured composite with polypyrrole coating (NiCo-LDH@PPy) was fabricated using NiCo-LDH as the substrate.The overpotential of NiCo-LDH@PPy-100 achieved 210.7 mV and 360.2 mV for HER and OER current density of 50 mA cm^{-2}, with overpotentials of only In 1 M KOH electrolyte, respectively. Furthermore, when NiCo-LDH@PPy-100 was employed as both cathode and anode, the decomposition voltage was only 1.61 V. The catalyst demonstrated excellent stability during a prolonged 50-h stability test. In seawater solution at a current density of 50 mA cm^{-2}, the NiCo-LDH@PPy-100 electrode material exhibits HER and OER overpotentials of 223.7 mV and 270.1 mV, respectively. For overall seawater splitting, this electrode material achieves a current density of 10 mA cm^{-2} at an applied voltage of 1.64 V. Furthermore, the NiCo-LDH@PPy-100 electrocatalyst maintains remarkable stability during seawater testing. The formation of the PPy composite structure significantly enhances both electrochemical activity and stability, thereby providing an excellent reference case for the industrial hydrogen production sector.

CRediT authorship contribution statement

Ziqi Wang: Writing – review & editing, Writing – original draft. **Xiaomei Wang:** Writing – review & editing, Writing – original draft. **Zhihao Xia:** Writing – review & editing. **Tian Tian:** Writing – review & editing. **Yucai Li:** Writing – review & editing. **Shiwei Song:** Writing – review & editing. **Jian Wang:** Writing – review & editing, Conceptualization. **Fang Hu:** Writing – review & editing, Conceptualization. **Lihua Miao:** Writing – review & editing.

Declaration of competing interest

The authors declare that they have no known competing financial interests or personal relationships that could have appeared to influence

the work reported in this paper.

Acknowledgment

This study was financially supported by the Natural Science Foundation Project of Science and Technology Department of Liaoning Province (2023-MS-247), College student innovation project (D202504251905128816, D202504252301176596), Science and Technology Innovation Talent Project of Liaoning Provincial Department of Education (LJ222411632049, LJ222411632081), Key Project of Liaoning Provincial Department of Education(LJKZZ20220141, LJKZZ20220140, LJKZ1084), Basic Scientific Research Project of Liaoning Provincial Department of Education(JYTMS20230305), Liaoning Province Science and Technology Plan Joint Program (2023JH2/101700265, 2023JH2/101700251).

References

[1] J.A. Dowling, K.Z. Rinaldi, T.H. Ruggles, S.J. Davis, M. Yuan, F. Tong, N.S. Lewis, K. Caldeira, Role of long-duration energy storage in variable renewable electricity systems, Joule 4 (9) (2020) 1907–1928.
[2] T. Jiang, D. Shen, Z. Zhang, H. Liu, G. Zhao, Y. Wang, S. Tan, R. Luo, W. Chen, Battery technologies for grid-scale energy storage, Nat. Rev. Clean Technol. 1 (7) (2025) 474–492.
[3] E. Rivard, M. Trudeau, K. Zaghib, Hydrogen storage for mobility: A review, Materials 12 (12) (2019) 1973.
[4] S. Ayca, I. Dincer, Life cycle environmental impact assessment and review of hydrogen fuels obtained from various sources for vehicles, Int. J. Hydrogen Energy 127 (2025) 265–274.
[5] A. Ganter, T.H. Ruggles, P. Gabrielli, G. Sansavini, K. Caldeira, Utilizing curtailed wind and solar power to scale up electrolytic hydrogen production in Europe, Environ. Sci. Technol. 59 (7) (2025) 3495–3507.
[6] S.W. Boettcher, Introduction to green hydrogen, Chem. Rev. 124 (23) (2024) 13095–13098.
[7] C. Rong, X. Huang, H. Arandiyan, Z. Shao, Y. Wang, Y. Chen, Advances in Oxygen Evolution Reaction Electrocatalysts via Direct Oxygen–Oxygen Radical Coupling Pathway, Adv. Mater. 37 (9) (2025) 2416362.
[8] R. Martínez-Hincapié, J. Timoshenko, T. Wagner, E. Ortega, J. Druce, M.C. O. Monteiro, M. Rüscher, J. Jang, E.Ö. Alagöz, S. Lasagna, L. Jacobse, A. Bergmann, B.R. Cuenya, S.Z. Oener, Interfacial solvation pre-organizes the transition state of the oxygen evolution reaction, Nat. Chem. (2025), https://doi.org/10.1038/s41557-025-01932-7.
[9] M. Yu, E. Budiyanto, H. Tüysüz, Principles of water electrolysis and recent Progress in cobalt-, nickel-, and Iron-based oxides for the oxygen evolution reaction, Angew. Chem. Int. Ed. 61 (1) (2021) e202103824.
[10] C. Minke, M. Suermann, B. Bensmann, R. Hanke-Rauschenbach, Is iridium demand a potential bottleneck in the realization of large-scale PEM water electrolysis? Int. J. Hydrogen Energy 46 (46) (2021) 23581–23590.
[11] Z.-Y. Wu, F.-Y. Chen, B. Li, S.-W. Yu, Y.Z. Finfrock, D.M. Meira, Q.-Q. Yan, P. Zhu, M.-X. Chen, T.-W. Song, Z. Yin, H.-W. Liang, S. Zhang, G. Wang, H. Wang, Non-iridium-based electrocatalyst for durable acidic oxygen evolution reaction in proton exchange membrane water electrolysis, Nat. Mater. 22 (1) (2022) 100–108.
[12] B.H.R. Suryanto, Y. Wang, R.K. Hocking, W. Adamson, C. Zhao, Overall electrochemical splitting of water at the heterogeneous interface of nickel and iron oxide, Nat. Commun. 10 (1) (2019) 5599.
[13] Y.-T. Zeng, M.-Y. Xu, T. Wang, S.-Y. Wu, J. Zhang, S.-C. Mu, J. Yu, Ru-decorated cobalt-iron oxide nanosheet arrays derived from MOF and LDH double-precursors for overall water splitting in alkali and seawater, Electrochim. Acta 444 (2023) 142004.
[14] C. Wang, Q. Geng, L. Fan, J.-X. Li, L. Ma, C. Li, Phase engineering oriented defect-rich amorphous/crystalline RuO2 nanoporous particles for boosting oxygen evolution reaction in acid media, Nano Res. Energy 2 (2023) e9120070.
[15] J. Zhang, K. Zhang, J. Yang, G.H. Lee, J. Shin, V. Wing-hei Lau, Y.M. Kang, Bifunctional conducting polymer coated CoP core–shell nanowires on carbon paper as a free-standing anode for sodium ion batteries, Adv. Energy Mater. 8 (20) (2018) 1800283.
[16] A. Raveendran, M. Chandran, R. Dhanusuraman, A comprehensive review on the electrochemical parameters and recent material development of electrochemical water splitting electrocatalysts, RSC Adv. 13 (6) (2023) 3843–3876.
[17] C. Wang, H. Yang, Y. Zhang, Q. Wang, NiFe alloy nanoparticles with hcp crystal structure stimulate superior oxygen evolution reaction Electrocatalytic activity, Angew. Chem. Int. Ed. 58 (18) (2019) 6099–6103.
[18] R. Shi, J. Wang, Z. Wang, T. Li, Y.-F. Song, Unique NiFe NiCoO2 hollow polyhedron as bifunctional electrocatalysts for water splitting, J. Energy Chem. 33 (2019) 74–80.
[19] D. Tyndall, S. Jaskaniec, B. Shortall, A. Roy, L. Gannon, K. O'Neill, M.P. Browne, J. Coelho, C. McGuinness, G.S. Duesberg, V. Nicolosi, Postsynthetic treatment of nickel–iron layered double hydroxides for the optimum catalysis of the oxygen evolution reaction, npj 2D, Materials Appl. 5 (1) (2021) 73.
[20] L. Jiang, X. Chen, L. Jiang, X. Luo, R. Li, Q. Zhou, X. Mu, L. Chen, J. Yu, S. Mu, Oxyanion-triggered discrepant oxide pathways via tailoring reconstruction of non-Noble catalysts for water oxidation, Nano Lett. 25 (37) (2025) 13875–13884.
[21] M. Xiao, C. Wu, J. Zhu, C. Zhang, Y. Li, J. Lyu, W. Zeng, H. Li, L. Chen, S. Mu, In situ generated layered NiFe-LDH/MOF heterostructure nanosheet arrays with abundant defects for efficient alkaline and seawater oxidation, Nano Res. 16 (7) (2023) 8945–8952.
[22] Y. Wu, X. Du, X. Zhang, Fe-doped CoMoO4/Ni3S2 grown on Ni foam as a multifunctional electrode for electrocatalytic seawater and urea splitting, J. Alloys Compd. 1030 (2025) 180927.
[23] Y. Wang, S. Liu, X. Du, X. Zhang, Controlled synthesis of co–Ni3Se2/MoS2/Ni3S2 nanoarrays as robust electrocatalyst for urea and seawater oxidation reaction, Int. J. Hydrogen Energy 88 (2024) 450–461.
[24] Y. Sun, Z. Zhao, Z. Wang, Y. Guo, Anion-exchange membrane water electrolysis: synergistic advances from material design to device integration, Functional Thin Films Energy Materials 1 (2025) 65–87.
[25] Y. Wu, X. Du, X. Zhang, P doping transition metal sulfides as bifunctional electrocatalyst for overall seawater splitting, Int. J. Hydrogen Energy 103 (2025) 174–182.
[26] L. Zhao, K. Meng, Y. Guo, Q. Wu, Q. Zhu, T. Zhou, Y. Fu, M. Wen, FeCoP sub-nanometric-sheets for electrocatalzing overall water splitting, Nano Res. Energy 3 (4) (2024) e9120129.
[27] J. Corbin, M. Jones, C. Lyu, A. Loh, Z. Zhang, Y. Zhu, X. Li, Challenges and progress in oxygen evolution reaction catalyst development for seawater electrolysis for hydrogen production, RSC Adv. 14 (9) (2024) 6416–6442.
[28] Y. Zhang, Z. Zhang, X. Zhang, J. Li, R. Guo, Research progress on NiCo-LDH electrocatalysts for oxygen evolution reaction, Int. J. Hydrogen Energy 102 (2025) 304–320.
[29] K. Khadija Tul, F. Noreen, A. Junaid, A. Nazir, S. Arshad, K. Bibi, A. Batool, A. Sattar, A.A. Awadh Bahajjaj, S. Ahmad, M.S. Khand, S.I. Abbas Shah, An effective bi-functional electrocatalyst for electrochemical water splitting using NiCo2O4 nanoparticles decorated with Polypyrrole nanocomposite, Fuel 397 (2025) 135381.
[30] D. Zhao, M. Dai, H. Liu, X. Zhu, X. Wu, PPy film anchored on ZnCo2O4 nanowires facilitating efficient bifunctional electrocatalysis, Materials Today Energy 20 (2021) 100637.
[31] R. Chércoles Asensio, M. San Andrés Moya, J.M. De La Roja, M. Gómez, Analytical characterization of polymers used in conservation and restoration by ATR-FTIR spectroscopy, Anal. Bioanal. Chem. 395 (7) (2009) 2081–2096.
[32] K. Fan, H. Chen, Y. Ji, H. Huang, P.M. Claesson, Q. Daniel, B. Philippe, H. Rensmo, F. Li, Y. Luo, L. Sun, Nickel–vanadium monolayer double hydroxide for efficient electrochemical water oxidation, Nat. Commun. 7 (1) (2016) 11981.
[33] M. Jia, C. Choi, T.-S. Wu, C. Ma, P. Kang, H. Tao, Q. Fan, S. Hong, S. Liu, Y.-L. Soo, Y. Jung, J. Qiu, Z. Sun, Carbon-supported Ni nanoparticles for efficient CO2 electroreduction, Chem. Sci. 9 (47) (2018) 8775–8780.
[34] S. Li, R. Ma, J. Hu, Z. Li, L. Liu, X. Wang, Y. Lu, G.E. Sterbinsky, S. Liu, L. Zheng, J. Liu, D. Liu, J. Wang, Coordination environment tuning of nickel sites by oxyanions to optimize methanol electro-oxidation activity, Nat. Commun. 13 (1) (2022) 2916.
[35] B. Laïk, M. Richet, N. Emery, S. Bach, L. Perrière, Y. Cotrebil, V. Russier, I. Guillot, P. Dubot, XPS Investigation of Co–Ni Oxidized Compounds Surface Using Peak-On-Satellite Ratio. Application to Co20Ni80 Passive Layer Structure and Composition, ACS Omega 9 (39) (2024) 40707–40722.
[36] M.M. Patwary, S. Haque, P. Szwedo, G. Hasan, R.S. Kondrapolu, F. Watanabe, K. Kc, D. Wang, A. Ghosh, Exploring enhanced oxygen reduction reactions: a study on Nanocellulose, dopamine, and cobalt complex-derived non-precious Electrocatalyst, Catalysts 14 (9) (2024) 613.
[37] Y. Wu, R. Sun, J. Cen, Facile synthesis of cobalt oxide as an efficient Electrocatalyst for hydrogen evolution reaction, Front. Chem. 8 (2020) 386.
[38] J. Xie, J. Du, P. Chen, G. Wang, J. Zhang, X. Yang, A. Kong, F. Yu, A facile route of Ti decoration for modulating M–O–Ti (M = Ni, Co) and oxygen vacancies on NiCo-LDH electrocatalysts for efficient oxygen evolution reaction, Indus. Chem. & Materials 3 (3) (2025) 342–352.
[39] Y. Liu, Y. Bai, Y. Han, Z. Yu, S. Zhang, G. Wang, J. Wei, Q. Wu, K. Sun, Self-supported hierarchical FeCoNi-LTH/NiCo2O4/CC electrodes with enhanced bifunctional performance for efficient overall water splitting, ACS Appl. Mater. Interfaces 9 (42) (2017) 36917–36926.
[40] S.V. Devaguptapu, S. Hwang, S. Karakalos, S. Zhao, S. Gupta, D. Su, H. Xu, G. Wu, Morphology control of carbon-free spinel NiCo2O4 catalysts for enhanced bifunctional oxygen reduction and evolution in alkaline media, ACS Appl. Mater. Interfaces 9 (51) (2017) 44567–44578.
[41] T. Zhou, Z. Cao, P. Zhang, H. Ma, Z. Gao, H. Wang, Y. Lu, J. He, Y. Zhao, Transition metal ions regulated oxygen evolution reaction performance of Ni-based hydroxides hierarchical nanoarrays, Sci. Rep. 7 (1) (2017) 46154.
[42] J. Fan, X. Qin, W. Jiang, X. Lu, X. Song, W. Guo, S. Zhu, Interface-coupling of NiFe-LDH on exfoliated black phosphorus for the high-performance Electrocatalytic oxygen evolution reaction, Front. Chem. 10 (2022) 951639.